DOI: 10.1002/ejic.201100201

Disorder in Rare Earth Metal Halide Carbide Nitrides

Manuel C. Schaloske,[a] Lorenz Kienle,[b] Hansjürgen Mattausch,[a] Viola Duppel,[a] and Arndt Simon*[a]

Dedicated to Professor John D. Corbett on the occasion of his 85th birthday

Keywords: Rod packing / Rare earths / Carbide nitrides / Disorder / X-ray diffraction / Electron microscopy

Single-crystal X-ray structure determinations of Ce_4I_6CN and disordered $Ce_6I_9C_2N$ phases are described together with electron-microscopy studies of $Ce_6I_9C_2N$ and $Y_6I_9C_2N$. Ce_4I_6CN crystallizes in the tetragonal space group $P4_2/mnm$ with $a = 13.877(2)$ Å, $c = 9.665(2)$ Å. Compounds β′-$Ce_6I_9C_2N$ and β′′-$Ce_6I_9C_2N$ crystallize in space group $P6/m$ with $a = 41.774(6)$ Å, $c = 13.719(3)$ Å and $a = 20.958(3)$ Å, $c = 13.793(3)$ Å, respectively. The main structural feature of these compounds are rods of RE_6C_2 octahedra and RE_4N tetrahedra (RE = lanthanide) interconnected in different sequences. These rods are linked into Kagomé-type frameworks with additional rods located in the centres of the hexagonal channels. The disorder patterns for these additional rods can be rationalized in terms of nearest-neighbour interactions.

Introduction

Structural frustration in rod-packing arrangements is analogous to frustration effects in antiferromagnetic systems. Like the spins in a triangular Ising net, rods with periodic contours may arrange randomly. Such disorder has been studied in great detail for the structure of $Na_{22}Ba_{14}CaN_6$ that contains a hexagonal close-packing array of rods, of composition $Na_6Ba_{14}CaN_6$, inserted into a honeycomb host structure formed by sodium atoms.[1] In spite of distinctly different structural features, closely related frustration effects are observed in rare-earth metal carbide nitride halides composed of C_2-centred RE_6 octahedra and N-centered RE_4 tetrahedra (RE = rare earth). These polyhedra can be connected in various sequences to form infinite rods or rod fragments.

In the following discussion two types of rods are essential and are depicted in Figure 1. The first is composed of alternating single octahedra and double tetrahedra, $^1_\infty$[ott]. The rods are aligned parallel in the structure of β-Gd_4I_6CN to form a Kagomé-type arrangement of triangles and hexagons with additional rods in the centres of the hexagonal channels, and every third rod of the latter type is rotationally disordered.[2] The second type of rods is formed from alternating double octahedra and double tetrahedra, $^1_\infty$[oott], and occurs in phases structurally characterized as $Y_6I_9C_2N$[2] and $Dy_6(C_2)OI_9$.[3]

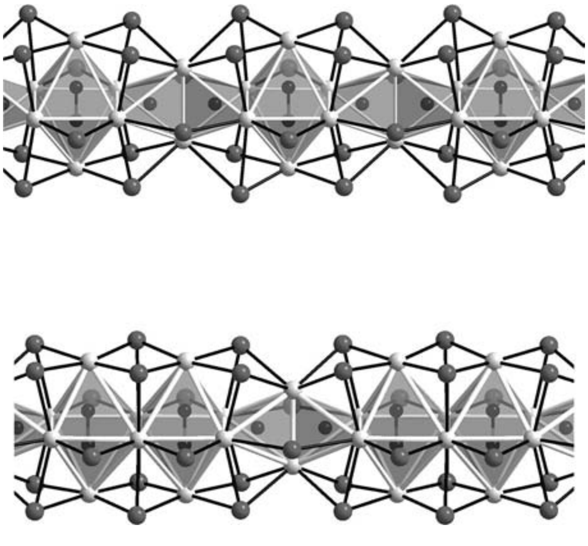

Figure 1. Top: side view of a rod in $(C_2)(N)_2Ce_8I_6$, notation: $^1_\infty$[ott]; bottom: a rod in $(C_2)_2(N)_2Ce_{12}I_{18}$, notation: $^1_\infty$[oott].

Herein we report two structural variants of $Ce_6I_9C_2N$, which show different degrees of disorder on the micro- and nanoscale. Moreover, we compare the structures of $Ce_6I_9C_2N$ and $Y_6I_9C_2N$ with the aid of a combined approach involving transmission electron microscopy, electron diffraction, and X-ray diffraction studies.

---

[a] Max-Planck-Institut für Festkörperforschung,
Heisenbergstr. 1, 70569 Stuttgart, Germany
Fax: +49-711-689-1091
E-mail: A.Simon@fkf.mpg.de
[b] Institut für Materialwissenschaft, Universität Kiel,
24143 Kiel, Germany

Results and Discussion

The metrics of the hexagonal structures of the phases with compositions $Ce_6I_9C_2N$ and Ce_4I_6CN are closely related and mainly differ by a stepwise change in the degree of structure disorder. Ce_4I_6CN is isostructural with β-Gd_4I_6CN,[4] and in the following rationalization of the increase in disorder, found for the two forms of $Ce_6I_9C_2N$ with respect to β-Gd_4I_6CN, these forms will be denoted as β′ and β′′.

A common feature of the structures is the Kagomé-type pattern depicted in Figure 2. This structural feature seems to be identical in all compounds when projected along [001] even though the compound constituents are different, namely $^1_\infty$[ott]-type rods in Ce_4I_6CN and $^1_\infty$[oott]-type rods in the case of $Ce_6I_9C_2N$. The rods are connected by iodine bridges. The atomic positions with respect to the *c* axis are identical for the different rods, and the connections are exclusively between the apices of the octahedra in one rod and the waists of the octahedra in an adjacent rod (X^{a-i}-type connection). The most disordered compound is β′′-$Ce_6I_9C_2N$ (Figure 3a), which may serve as an example to highlight some structural details that are common to these compounds: The Ce–I distances in the bridges are 3.38 Å. The distances to surrounding I atoms are in the range of 3.20–3.40 Å, with the longest distances occurring around the tetrahedral units. Within the rods the range of Ce–Ce distances is widely spread. Whereas the connecting edges between adjacent clusters are significantly short (3.37–3.59 Å), the other distances vary between 3.91 and 4.16 Å. The rods incorporated in the hexagonal tubes of the Kagomé-type framework are shifted by *c*/2 with respect to the framework. Thus, the octahedra in the rods are next to the tetrahedra in the framework. The Ce–Ce distances as well as the Ce–I distances associated with the inserted rods lie in the same ranges as those of the framework bonds (3.40–3.93 Å and 3.08–3.39 Å, respectively).

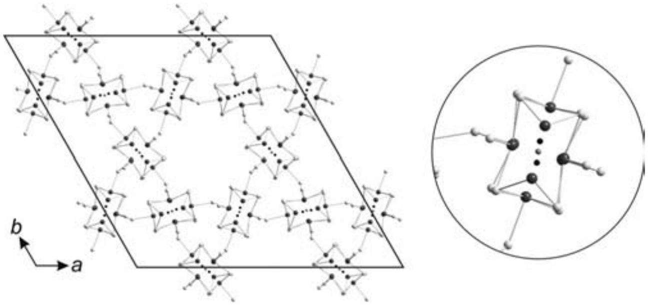

Figure 2. Projection along [001] of the Kagomé-type substructure of $Ce_6I_9C_2N$. The I, Ce, N and C atoms are drawn as bright grey, dark grey, light grey and black spheres, respectively; Ce–I bonds are shown as sticks. A close-up view of one of the stuctural units is shown on the right of the diagram.

Whereas all inserted rods in β′′-$Ce_6I_9C_2N$ show threefold disorder through rotation by 120°, the average structure of β′-$Ce_6I_9C_2N$ exhibits an alternation of a superposition of three and two rods in the hexagonal channels of the framework (see Figure 3b). The average structure of β′-$Ce_6I_9C_2N$ has the same space group (*P*6/*m*) with almost the same *c* lattice parameter, but with a doubled *a* value, as β′′-$Ce_6I_9C_2N$.

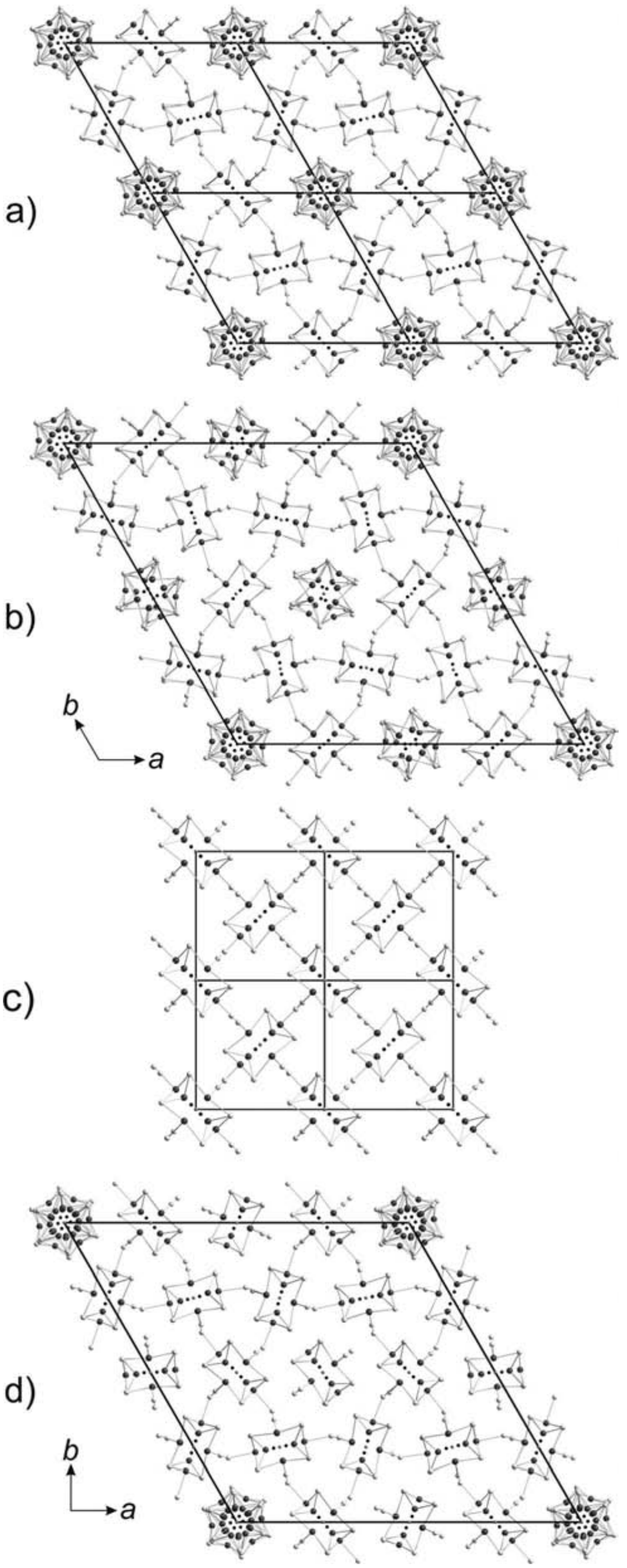

Figure 3. Projections along [001] of (a) β′′-$Ce_6I_9C_2N$, (b) β′-$Ce_6I_9C_2N$, (c) Ce_4I_6CN and (d) β-Gd_4I_6CN. Atoms drawn as in Figure 2.

Evidently, the threefold disordered rods in the structures of β′′- and β′-$Ce_6I_9C_2N$ refine with atomic occupancy factors of 1/3. However, the rods in β′-$Ce_6I_9C_2N$ that are located on the twofold axes can be refined independently; occupancies of 1/2, within error, result for the Ce and I atoms. A third possible orientation of the rod is entirely missing. Interatomic distances within β′-$Ce_6I_9C_2N$ are similar to those in β′′-$Ce_6I_9C_2N$.

In addition to the two variants of $Ce_6I_9C_2N$, the quaternary compound Ce_4I_6CN was also found in the product mixture. Two rod structures have been identified within the phases of the compound with composition Gd_4I_6CN. Whereas in the tetragonal structure of α-Gd_4I_6CN all rods are fixed (Figure 3c), the hexagonal structure of β-Gd_4I_6CN contains threefold disordered rods situated in the hexagonal tubes of the Kagomé-type framework. The threefold disorder of one type of inserted rods is the same as in $Ce_6I_9C_2N$, whereas every second rod is ordered (Figure 3d). In the case of Ce_4I_6CN only the tetragonal, and fully ordered, variant could be identified. The Ce–Ce distances in this compound vary between 3.54 and 4.00 Å, and the Ce–I distances are in the range of 3.20–3.60 Å.

In contrast to the refinement of the ordered (tetragonal) structure of Ce_4I_6CN, the results for the disordered (hexagonal) structures of $Ce_6I_9C_2N$ are poor (see Table 1). The unconvincing agreement between the calculated and observed intensities is in part due to the quality of the crystals that easily split into fibers. However, the disagreement has a more intricate origin as indicated by the spread of R values calculated for the hkl layers with varying l values for the β′′-$Ce_6I_9C_2N$ XRD data. Whereas $R_1 = 0.03$ for the $l = 0$ layer, the corresponding values for the other layers range between 0.10 and 0.24. Thus, only the projection along the rod packing is well defined, which gives evidence for a translational disorder of the rods in addition to the rotational disorder or even a compositional variation due to sequences other than $^{1}_{\infty}$[oott].

Since high-resolution transmission electron microscopy (HRTEM) enables a local view of the structure by nanofocusing, the averaging effects inherent to XRD methods should be reduced. The crystallites are strongly textured with the preferred habit being very thin needles that grow along the [001] direction. When crushed, these needles split into thin fibers with high aspect ratios and preferred orientation [uv0]. Due to the limited tilting range for the sample caused by the confined space between the objective lens pole pieces, the electron microscopy examinations are limited to the [uv0] directions, e.g. [100]. Along this zone axis the rods are superimposed to give the impression of sheets parallel to (010). These sheets appear with different contrasts. According to numerous model calculations, this effect is due to preferred orientations of the rods within a sheet but changing orientations between sheets. Thus, the partially ordered structure of β′-$Ce_6I_9C_2N$ can be discerned from that of β′′-$Ce_6I_9C_2N$ by the separation of consecutive sheets containing twofold- and threefold disorder that

Table 1. Crystal data and structure-refinement details for β′′-, β′-$Ce_6I_9C_2N$ and Ce_4I_6CN.

	β′′-$Ce_6I_9C_2N$	β′-$Ce_6I_9C_2N$	Ce_4I_6CN
Formula mass [g mol^{-1}]	2020.85	2020.85	1347.90
Crystal colour, habit	black, lath	black, lath	brown, needle
T [K]	293(2)	293(2)	293(2)
λ [Å]	0.71073 (Mo-K_α)	0.71073 (Mo-K_α)	0.71073 (Mo-K_α)
Crystal system	hexagonal	hexagonal	tetragonal
Space group	$P6/m$	$P6/m$	$P4_2/mnm$
Cell dimensions [Å]	a = 20.958(3) c = 13.793(3)	a = 41.774(6) c = 13.719(3)	a = 13.877(2) c = 9.665(2)
V [Å^3]	5246.7(16)	20734(6)	1861.3(5)
Z	8	32	4
$\rho_{calcd.}$ [g cm^{-3}]	5.117	5.179	4.810
μ [mm^{-1}]	20.769	21.023	19.516
F(000)	6752	27008	2252
Crystal dimension [mm]	0.13 × 0.05 × 0.04	0.16 × 0.08 × 0.07	0.25 × 0.08 × 0.06
Diffractometer	IPDS II (Stoe, Darmstadt)	IPDS II (Stoe, Darmstadt)	IPDS II (Stoe, Darmstadt)
θ range [°]	$2.25 \leq \theta \leq 28.43$	$1.78 \leq \theta \leq 31.80$	$2.94 \leq \theta \leq 31.17$
Index ranges	$-31 \leq h \leq 26$ $-29 \leq k \leq 29$ $-20 \leq l \leq 20$	$-54 \leq h \leq 54$ $-54 \leq k \leq 54$ $-16 \leq l \leq 17$	$-19 \leq h \leq 20$ $-20 \leq k \leq 20$ $-12 \leq l \leq 14$
Reflections measured/independent	64087/6288	254996/24662	21642/1783
Absorption correction	none	numerical[5]	numerical[5]
Max./min. transmission		0.0812/0.0150	0.4220/0.1204
Structure solution	direct methods[6]	direct methods[6]	direct methods[6]
Structure refinement	full-matrix least squares on F^2[5]	full-matrix least squares on F^2[5]	full-matrix least squares on F^2[5]
Data/parameters	1422/143	8473/539	1374/41
Goodness-of-fit on F^2	1.052	1.066	1.307
R values [$I \geq 2\sigma(I)$]	$R1$ = 0.1686, $wR2$ = 0.1871	$R1$ = 0.1774, $wR2$ = 0.3973	$R1$ = 0.0740, $wR2$ = 0.1323
R values (all data)	$R1$ = 0.3630, $wR2$ = 0.2614	$R1$ = 0.2701, $wR2$ = 0.4613	$R1$ = 0.0900, $wR2$ = 0.1369
Final Fourier residuals [e Å^{-3}]	2.803/–3.967	8.964/–9.590	2.651/–1.994

correspond to β′- and β′′-$Ce_6I_9C_2N$, respectively. The presence of structural variants, particularly the superstructure for β′-$Ce_6I_9C_2N$ is not only evident from the high-resolution imaging data but also from the electron-diffraction data. The selected-area electron diffraction (SAED) patterns shown in Figure 4a were recorded on β′′-$Ce_6I_9C_2N$ (left) and β′-$Ce_6I_9C_2N$ (right). A row of reflections in the pattern of β′-$Ce_6I_9C_2N$ shows doubling of the *a* and *b* axes compared to the metrics of β′′-$Ce_6I_9C_2N$ (left). The HRTEM micrographs in Figure 4b exhibit slight differences in the phase contrasts of the two structures. Line scans within the marked areas of Figure 4b highlight the specific periodicities of the structures along <210>. In the pattern of β′′-$Ce_6I_9C_2N$ (Figure 4b, left) all peaks indicated with arrows have the same intensity, whereas in the pattern for β′-$Ce_6I_9C_2N$ alternating intensity maxima occur. These distinct periodicities are also visible in the Fourier transforms of the micrographs (not shown) that contain superstructure peaks for β′-$Ce_6I_9C_2N$, i.e. *hkl* reflections with $k = n/2$.

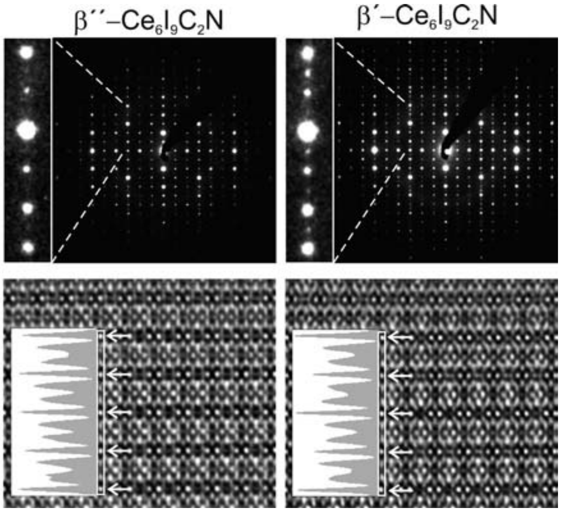

Figure 4. Comparison of SAED patterns with enlarged sections (a) and HRTEM micrographs (b), $\Delta f \approx -30$ nm, with line scans (insets) for β′′-$Ce_6I_9C_2N$ (left) and β′-$Ce_6I_9C_2N$ (right). The zone axes are along [100].

These differences in contrast cannot just be assigned to changes in the metrics of the compounds, but the specific structural features of β′′- and β′-$Ce_6I_9C_2N$ must also be considered. According to the simulated micrographs shown in Figure 5a, the partial ordering of the β′-$Ce_6I_9C_2N$ structure (Figure 5a, right) produces alternating bright and dark contrasts for the sheets seen in the micrograph (indicated by horizontal arrows), due to the superposition of twofold- and threefold disordered rods, respectively. In the case of β′′-$Ce_6I_9C_2N$ (Figure 5a, left) such contrast differences fade since all adjacent sheets contain rods with only threefold disorder. The complete atomic ordering within the rods, particularly the presence of the cluster sequence $^1_\infty$[oott], is indicated by the periodicity of the structural motifs along the *c* axis, as indicated by the vertical arrows. The series of images recorded with variable foci that are shown in Figure 5b allows for comparison of experimentally obtained and simulated micrographs that are based on the average structure models. Even in the case of the image recorded with a strongly under-focused beam the simulation correlates well with the corresponding experimental micrograph; however, a perfect match cannot be achieved when applying an average model in the simulation.

In exceptional cases an intergrowth of both structural variants was observed. In this case, the [100] SAED patterns show diffuse streaks along *b** between the main reflections. The intergrowth is clearly observable in the HRTEM micrographs (Figure 6). While in the upper part of the image the typical sequence of sheets corresponding to the β′′-$Ce_6I_9C_2N$ structure is present, the lower part shows alternating contrast for the sheets, corresponding to the partial ordering of the β′-$Ce_6I_9C_2N$ structure. The Fourier transforms (not shown) calculated for both sides of the phase boundary seen in the image support such an assignment due to the lack of superstructure peaks for *hkl* reflections with $k = n/2$.

An extension of the real structure model based on two-dimensional disorder with rods ordered in themselves is found for samples with the nominal composition $Y_6I_9CN_2$. In this case, the [100] SAED patterns show diffuse streaks between the main reflections along *b** (see Figure 7a, left). Patterns with concentrations of diffuse intensity associated with *hkl* reflections with $k = n/2$ were observed, indicating that these compounds have partial order like in β′-$Ce_6I_9C_2N$ (Figure 7a, centre). Surprisingly, many crystallites exhibit structural disorder along the rod axes. In this case, the bright-field images (Figure 7b) display broad modulation waves (highlighted by arrows in Figure 7b) that propagate along the *c* axes, and the corresponding SAED patterns (Figure 7a, right) contain split reflections. The formation of modulation waves strongly suggests that these disorder phenomena are not restricted to single rods, but include neighboring rods in adjacent (010) sheets. HRTEM micrographs clearly show deviations from the sequence of clusters described for $Ce_6I_9C_2N$ (Figure 7c). For $\Delta f =$ +40 nm, the bright crosses correlate with the positions of the oo-type units, and the sequence along *c* is consistent with $^1_\infty$[oott] of the clusters on the left and right. In the centre of the pattern shown in Figure 7c, the sequence is disturbed as highlighted by the arrows. Such variations could be due to partially deviating periodic structures with complex sequences of the clusters, which might be accessible in discrete phases.

Finally, the question arises as to what causes the different degrees of disorder in the phases discussed. Possible answers include: (i) The distances in the Ce–I–Ce bridges within the Kagomé-type framework are approximately 0.3 Å shorter than those associated with the rods inserted in the hexagonal channels. Hence, the comparably weaker bonding in the latter case favours rotational disorder. (ii) There exists a triangular arrangement of contoured rods within each structure that have minima and maxima in diameter at identical heights along the *c* axes. A close packing of such rods can be optimized by mutually shifting them along the *c* axes to give a positional ratio 1:2 for each tri-

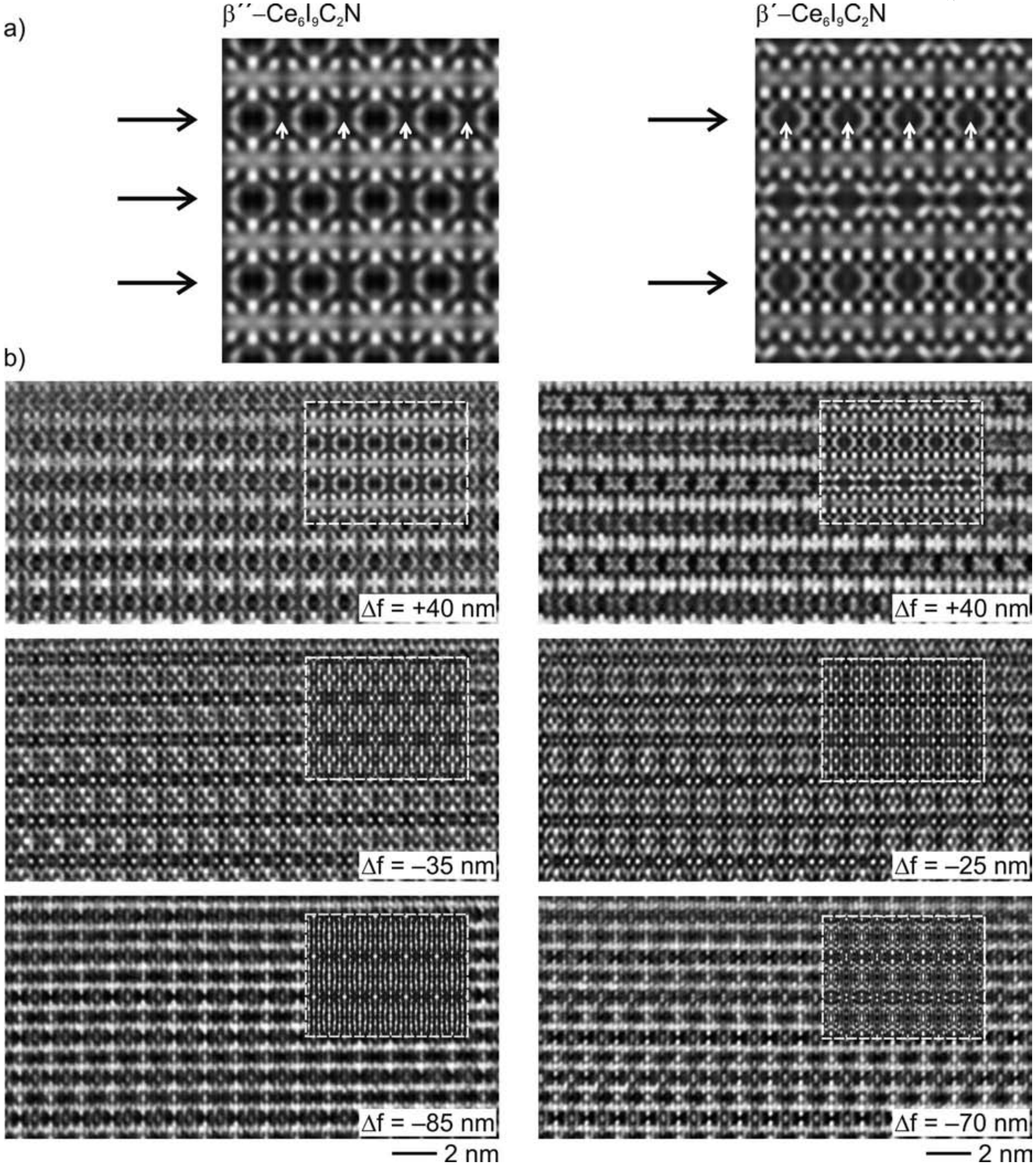

Figure 5. (a) Comparison of simulated micrographs based on the average structures of β′′-$Ce_6I_9C_2N$ (left) and β′-$Ce_6I_9C_2N$ (right); (b) series of HRTEM micrographs with different foci (Δ*f*) for β′′-$Ce_6I_9C_2N$ (left) and β′-$Ce_6I_9C_2N$ (right) with simulated micrographs (insets). All simulations were calculated on the basis of the average structures of β′′-$Ce_6I_9C_2N$ and β′-$Ce_6I_9C_2N$ (from X-ray diffraction analyses), the zone axes were along [100] and the crystal thickness was 8.4 nm.

angle. Such a condition corresponds to maximal frustration, and obviously partly occurs as indicated by the results of the structure refinement and the significant excess electron densities observed in the XRD analyses. (iii) The first coordination shell, the hexagonal channel, for all inserted rods is identical, no matter whether or not there is order or disorder of the rods. However, provided that the channel adjusts slightly to the respective rod orientation, then interaction within the triangular arrangement is possible, and the second coordination shell becomes important. (iv) Indeed, sketches of the ordering patterns are presented in Figure 8, and they give evidence for the influence, by symmetry, of the second coordination shells on the structures of β′- and β′′-$Ce_6I_9C_2N$ as well as Ce_4I_6CN. Figure 8d also presents a hypothetical case of total order for all rods inserted into a Kagomé-type framework.

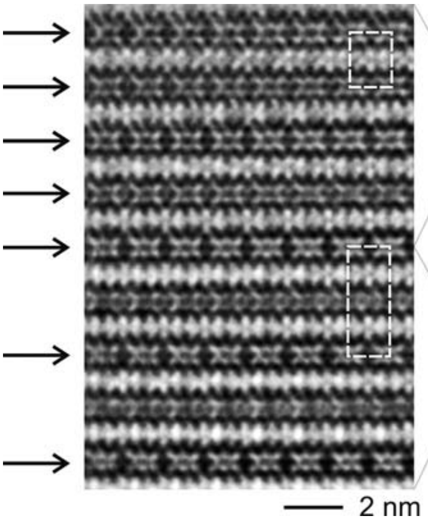

Figure 6. HRTEM micrograph recorded next to a boundary between β′′-$Ce_6I_9C_2N$ (top) and β′-$Ce_6I_9C_2N$ (bottom), $\Delta f \approx +40$ nm. Unit cells are shown as dashed lines.

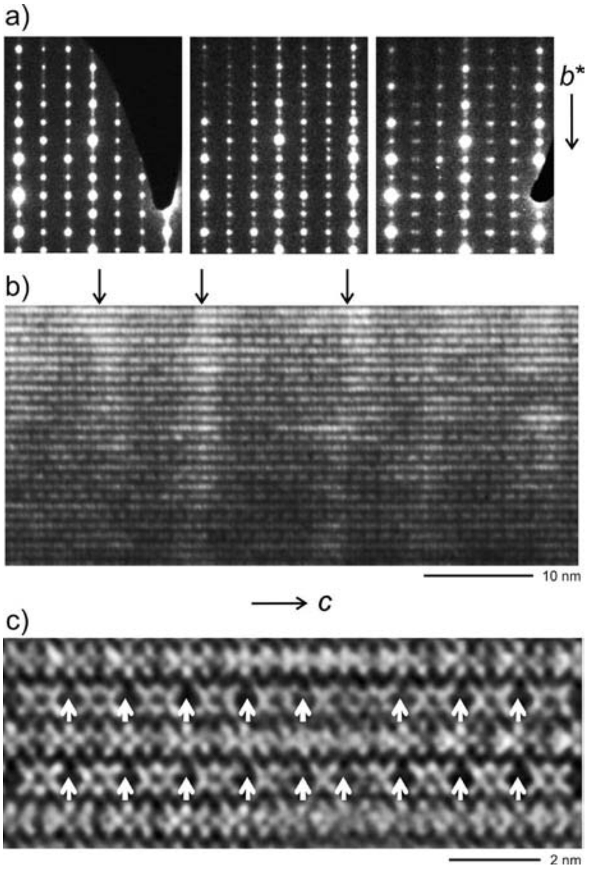

Figure 7. (a) SAED patterns recorded for $Y_6I_9C_2N$ showing diffuse streaks (left), concentrations of diffuse intensity for *hkl* reflections with $k = n/2$ (centre), and split reflections (right); (b) bright-field image; (c) HRTEM micrograph ($\Delta f \approx +40$ nm). All zone axes are along [100].

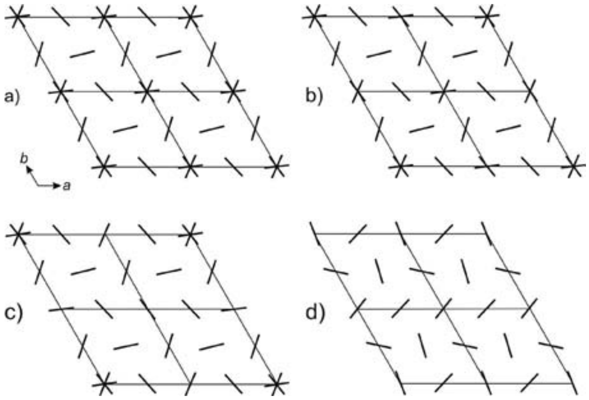

Figure 8. Schematic representation of the disorder patterns for the structures of (a) β′′-$Ce_6I_9C_2N$, (b) β′-$Ce_6I_9C_2N$, (c) β-Gd_4I_6CN and (d) $RE_6I_9C_2N$, which is hypothetically ordered. These diagrams can be compared with Figure 3.

Conclusions

The rare earth halide carbide nitrides structures reported herein are built from infinite rods consisting of edge-sharing tetrahedra and octahedra linked in the sequences $^1_\infty$[ott] and $^1_\infty$[oott]. These rods form Kagomé-type frameworks with additional rods filling the hexagonal channels. The structures appear to be disordered to different degrees due to interactions with the second-order coordination shells. Further reasons for the disorder may be frustration effects and statistical variations in the structures of the above mentioned sequences, as evidenced by X-ray diffraction analyses, which probe the average structures, and local-probe electron microscopy results.

Experimental Section

Synthesis: All procedures were carried out under argon either in a glove box (M. Braun) or with the Schlenk technique. Ce metal (sublimed, 99.99%, Alfa-Aesar), CeI_3, CeN and graphite powder were used as starting materials. CeI_3 was synthesized by dissolving Ce metal in an aqueous HI/NH_4I (Merck) solution,[7] which was then heated to dryness at 430 °C. The raw product was purified twice by sublimation in a Ta tube at 850 °C and under a reduced pressure of 10^{-5} Torr. CeN was prepared by heating Ce metal in a purified N_2 stream first at 750 °C (12 h), and then after grinding, at 1200 °C in an Mo boat (12 h). The product is stoichiometric with less than 2% N_2 deficit.[8] The graphite powder (Aldrich) was outgased at 1050 °C and 10^{-5} Torr. A mixture of Ce (0.139 g)/CeI_3 (0.773 g)/CeN (0.076 g)/C (0.012 g) in a 2:3:1:2 molar ratio was placed in Ta tubes that were arc-sealed under argon,[9] and then enclosed in silica ampoules in vacuo. The ampoules were annealed at 850 °C for 18 d and then quenched in water. Both forms of $Ce_6I_9C_2N$, phases β′ and β′′, were found in similar amounts in addition to Ce_4I_6CN in the resultant product mixture. The phases of $Ce_6I_9C_2N$ form soft black crystals that are lath-shaped and easily split into needles. The crystals are moisture-sensitive and decompose rapidly in humid air.

X-ray Structure Investigations: The reaction products were ground to fine powders under argon and sealed in glass capillaries for phase identification by a modified Guinier technique[10] (Cu-$K_{\alpha 1}$: λ = 1.54056 Å; internal standard Si with a = 5.43035 Å; Fujifilm BAS-5000 image-plate system). Single crystals were transferred to glass capillaries in Na-dried paraffin oil and sealed under argon. The crystals were first examined by the precession technique before being characterized with a Stoe IPDS image-plate instrument. The average structures of $\mathrm{Ce_6I_9C_2N}$ can be assigned to the same space group, $P6/m$, and have lattice parameters of a = 20.958(3) Å, c = 13.793(3) Å (β'-$\mathrm{Ce_6I_9C_2N}$) and a = 41.774(6) Å, c = 13.719(3) Å (β''-$\mathrm{Ce_6I_9C_2N}$). $\mathrm{Ce_4I_6CN}$ crystallizes in the space group $P4_2/mnm$ with a = 13.877(2) Å, c = 9.665(2) Å. The parameters for data collection and other crystallographic information are listed in Tables 1, 2, 3, and 4. Further details on the crystal structure investigations may be obtained from the Fachinformationszentrum Karlsruhe, 76344 Eggenstein-Leopoldshafen, Germany (Fax: +49-7247-808-666; E-mail: crysdata@fiz-karlsruhe.de), on quoting the depository number numbers CSD-421899 (β'-$\mathrm{Ce_6I_9C_2N}$), -421900 (β''-$\mathrm{Ce_6I_9C_2N}$) and -421901 ($\mathrm{Ce_4I_6CN}$).

Table 2. Wyckoff positions, atomic coordinates, displacement parameters [Å^2], and atomic occupancies for atoms in β''-$\mathrm{Ce_6I_9C_2N}$.

Atom	W.N.	x	y	z	U_{eq}	occ.
Ce1	12*l*	0.4734(2)	0.4043(2)	0.2832(2)	0.0352(9)	1
Ce2	12*l*	0.4600(2)	0.1216(2)	0.1582(2)	0.0316(8)	1
Ce3	6*j*	0.4710(3)	0.4092(3)	0	0.0269(12)	1
Ce4	6*k*	0.5944(3)	0.5231(4)	0.5	0.0386(14)	1
I1	12*l*	0.4262(3)	0.2629(3)	0.1463(2)	0.0424(11)	1
I2	6*j*	0.5840(4)	0.2138(4)	0	0.0325(15)	1
I3	6*j*	0.3305(4)	0.0414(4)	0	0.0314(15)	1
I4	12*l*	0.6362(3)	0.4301(3)	0.3344(3)	0.0497(13)	1
I5	12*l*	0.2995(3)	0.3467(3)	0.3347(3)	0.0591(15)	1
I6	6*k*	0.4495(5)	0.3228(4)	0.5	0.0501(19)	1
N1	6*i*	0.5	0.5	0.611(4)	0.018(13)	1
C1	12*l*	0.457(3)	0.489(3)	0.148(4)	0.028(12)	1
Ce5	6*k*	0.9415(9)	0.0342(12)	0.5	0.034(5)	0.33
Ce6	6*j*	0.0893(9)	0.0112(12)	0	0.040(5)	0.33
Ce7	12*l*	0.0400(6)	0.0988(7)	0.2177(7)	0.032(3)	0.33
Ce8	12*l*	–0.0203(6)	0.1330(5)	0.3414(6)	0.027(2)	0.33
I7	6*k*	0.0882(11)	0.2208(7)	0.5	0.088(6)	0.67
I8	12*l*	0.2069(4)	0.1251(5)	–0.1655(5)	0.060(2)	0.67
I9	12*l*	0.0935(7)	0.2324(6)	0.6423(8)	0.035(3)	0.33
I10	6*j*	0.1068(12)	–0.0702(12)	0	0.040(4)	0.33
N2	2*e*	0	0	0.106(7)	0.02(2)	1
C2	12*l*	0.0374	0.0384	0.362(7)	0.00(2)	0.33

Electron Microscopy: HRTEM, SAED and PED analyses were performed with a Philips CM30 ST microscope (300 kV, $\mathrm{LaB_6}$ cathode, C_S = 1.15 mm). All manipulations for the preparation and transfer of the samples were carried out under argon with the aid of a special device.[11] A perforated carbon/copper net served as a support for the crystallites. In the SAED mode, the aperture limited the diffraction zone to a circular area that was 250 nm in diameter. Simulations of the HRTEM images (multislice formalism) were calculated with the EMS program package[12] (defocus spread: 70 Å, illumination semi-angle: 1.2 mrad). All images were recorded with a Gatan Multiscan CCD camera and evaluated (including Fourier filtering) with the program Digital Micrograph 3.6.1 (Gatan). HRTEM images were filtered after Fourier transformation with a suitable band-pass mask. Elemental analyses, by energy-dispersive X-ray spectroscopy (EDX), were performed with the nanoprobe set in the CM30ST scanning mode and equipped with an Si/Li detector (Noran, Vantage System).

Table 3. Wyckoff positions, atomic coordinates, displacement parameters [Å^2], and atomic occupancies for atoms in β'-$\mathrm{Ce_6I_9C_2N}$.

Atom	W.P.	x	y	z	U_{eq}	occ.
Ce1	6*k*	0.7664(1)	0.4687(1)	0.5	0.0372(8)	1
Ce2	12*l*	0.8330(1)	0.5623(1)	0.3449(2)	0.0449(7)	1
Ce3	12*l*	0.9406(1)	0.7713(1)	0.3419(3)	0.0474(7)	1
Ce4	6*k*	0.9694(1)	0.7053(1)	0.5	0.0448(10)	1
Ce5	12*l*	0.7674(1)	0.4674(1)	0.2164(2)	0.0352(6)	1
Ce6	12*l*	0.7388(1)	0.5345(1)	0.2172(3)	0.0470(7)	1
Ce7	6*k*	0.7376(1)	0.5308(1)	0.5	0.0401(9)	1
Ce8	6*j*	0.7997(1)	0.5378(1)	0	0.0496(11)	1
Ce9	12*l*	0.0358(1)	0.7976(1)	0.2162(3)	0.0509(8)	1
Ce10	12*l*	0.6720(1)	0.4389(1)	0.3396(3)	0.0438(7)	1
Ce11	6*k*	0.0322(1)	0.7963(1)	0.5	0.0457(10)	1
Ce12	12*l*	0.9654(1)	0.7030(1)	0.2166(3)	0.0514(8)	1
Ce13	6*j*	0.7068(1)	0.4645(1)	0	0.0435(10)	1
Ce14	6*j*	0.9660(1)	0.7632(2)	0	0.0551(12)	1
Ce15	6*j*	0.0343(1)	0.7364(2)	0	0.0577(12)	1
Ce16	12*l*	0.0606(1)	0.7289(1)	0.3424(3)	0.0484(7)	1
Ce17	6*j*	0.9532(2)	0.4810(2)	0	0.030(2)	0.48(1)
Ce18	6*j*	0.9719(2)	0.4533(2)	0	0.031(2)	0.52(1)
Ce19	12*l*	0.9902(1)	0.4233(1)	0.1587(4)	0.0315(16)	0.47(1)
Ce20	12*l*	0.9330(1)	0.5105(1)	–0.1600(4)	0.0347(15)	0.53(1)
Ce21	12*l*	0.9704(1)	0.4505(1)	0.2828(4)	0.0310(15)	0.51(1)
Ce22	12*l*	0.9504(1)	0.4804(1)	–0.2826(4)	0.0294(15)	0.49(1)
Ce23	6*k*	0.0058(2)	0.5448(2)	0.5	0.036(2)	0.49(2)
Ce24	6*k*	0.9611(2)	0.5062(2)	0.5	0.037(2)	0.52(2)
Ce25	12*l*	0.9911(3)	0.9230(3)	0.1574(9)	0.052(2)	0.33
Ce26	6*j*	0.9712(4)	0.9527(4)	0	0.058(4)	0.33
Ce27	12*l*	0.9802(3)	0.0291(3)	0.2862(12)	0.067(3)	0.33
Ce28	6*k*	0.9935(5)	0.9548(4)	0.5	0.067(4)	0.33
I1	6*k*	0.9808(2)	0.8358(2)	0.5	0.0616(15)	1
I2	6*k*	0.8942(1)	0.7096(1)	0.5	0.0522(13)	1
I3	12*l*	0.9188(1)	0.6333(1)	0.3544(3)	0.0533(9)	1
I4	6*k*	0.8160(2)	0.6079(1)	0.5	0.0568(14)	1
I5	12*l*	0.8686(1)	0.7863(1)	0.3541(3)	0.0591(10)	1
I6	12*l*	0.9791(1)	0.8286(1)	0.1659(4)	0.0715(12)	1
I7	6*k*	0.8578(2)	0.5215(2)	0.5	0.0572(14)	1
I8	12*l*	0.6533(1)	0.4759(1)	0.1631(3)	0.0519(9)	1
I9	6*k*	0.6467(1)	0.4781(1)	0.5	0.0455(12)	1
I10	12*l*	0.8975(1)	0.7171(1)	0.1646(4)	0.0643(11)	1
I11	12*l*	0.6863(1)	0.3975(1)	0.1667(3)	0.0460(8)	1
I12	12*l*	0.7887(1)	0.4180(1)	0.3528(3)	0.0546(9)	1
I13	6*k*	0.6867(1)	0.3930(1)	0.5	0.0466(11)	1
I14	12*l*	0.8548(1)	0.5265(1)	0.1655(3)	0.0585(10)	1
I15	6*j*	0.7278(2)	0.5643(2)	0	0.0592(14)	1
I16	6*k*	0.0206(2)	0.6644(2)	0.5	0.0533(13)	1
I17	6*j*	0.0650(2)	0.8388(2)	0	0.0739(19)	1
I18	12*l*	0.8194(1)	0.6042(1)	0.1689(4)	0.0668(11)	1
I19	6*j*	0.7806(1)	0.4393(2)	0	0.0478(11)	1
I20	12*l*	0.0405(1)	0.4372(1)	0.3353(3)	0.0564(10)	1
I21	12*l*	0.7129(1)	0.5802(1)	0.6481(3)	0.0549(9)	1
I22	6*k*	0.7910(1)	0.6842(2)	0.5	0.0492(12)	1
I23	12*l*	0.0209(1)	0.6700(1)	0.1696(4)	0.0695(12)	1
I24	6*j*	0.9564(3)	0.5671(3)	0	0.085(3)	1
I25	6*j*	0.8897(2)	0.4471(2)	0	0.033(2)	0.51(2)
I26	6*j*	0.9255(2)	0.3912(2)	0	0.030(2)	0.49(2)
I27	12*l*	0.8954(2)	0.4513(2)	–0.3332(7)	0.052(2)	0.49(1)
I28	12*l*	0.9312(2)	0.3970(2)	0.3334(7)	0.056(3)	0.51(1)
I29	12*l*	0.9293(2)	0.3831(2)	0.1451(5)	0.0376(19)	0.50(1)
I30	12*l*	0.8829(2)	0.4535(2)	–0.1441(5)	0.039(2)	0.50(1)
I31	6*k*	0.0540(3)	0.5896(2)	0.5	0.041(3)	0.54(2)
I32	6*k*	0.9111(2)	0.4639(3)	0.5	0.036(3)	0.46(2)
I33	12*l*	0.1026(1)	0.7823(1)	0.1632(3)	0.0618(10)	1
I34	6*j*	0.9362(2)	0.6619(2)	0	0.0737(18)	1
I35	12*l*	0.9385(2)	0.8960(2)	0.3353(6)	0.076(2)	0.67
I36	6*k*	0.9481(5)	0.9124(6)	0.5	0.073(6)	0.33
I37	12*l*	0.9325(5)	0.8862(4)	0.080(5)	0.63(7)	0.67
N1	6*i*	0	0.5	–0.390(5)	0.042(12)	1
N2	2*e*	0	0	0.390(7)	0.031(18)	1
N3	12*l*	0.7530(8)	0.5001(8)	0.108(2)	0.022(6)	1
N4	12*l*	0.9991(17)	0.7509(17)	0.106(5)	0.077(16)	1
C1	12*l*	0.7705(15)	0.5164(15)	0.356(5)	0.051(12)	1
C2	12*l*	0.7359(9)	0.4894(9)	0.350(3)	0.017(6)	1
C3	12*l*	0.9885(12)	0.7575(12)	0.343(4)	0.036(9)	1
C4	12*l*	0.0128(13)	0.7432(13)	0.372(4)	0.042(11)	1
C5	12*l*	0.996(2)	0.016(2)	0.138(6)	0.000(15)	0.33
C6	12*l*	0.5190(13)	0.5166(12)	0.157(4)	0.000(9)	0.50
C7	12*l*	0.5084(14)	0.5216(13)	0.147(4)	0.002(9)	0.50

Table 4. Wyckoff positions, atomic coordinates and displacement parameters [Å^2] for atoms in Ce_4I_6CN.

Atom	W.P.	*x*	*y*	*z*	U_{eq}
Ce1	4*f*	0.4071(1)	0.4071(1)	0	0.0231(4)
Ce2	8*j*	0.0902(1)	0.0902(1)	0.1934(1)	0.0183(3)
Ce3	4*g*	0.8444(1)	0.1556(1)	0	0.0221(4)
I1	4*f*	0.2235(1)	0.2235(1)	0	0.0476(9)
I2	4*g*	0.6719(1)	0.3281(1)	0	0.0352(7)
I3	16*k*	0.2315(1)	0.4496(1)	0.2508(2)	0.0333(3)
C1	4*g*	0.9629(17)	0.0371(17)	0	0.019(6)
N1	4*e*	0	0	0.344(3)	0.015(5)

Acknowledgments

The authors are indebted to Dr. C. Hoch and H. Gärttling for the single-crystal X-ray investigations.

---

[1] U. Steinbrenner, A. Simon, *Z. Kristallogr.* **1997**, *212*, 428–438.

[2] H. Mattausch, H. Borrmann, R. Eger, R. K. Kremer, A. Simon, *Z. Anorg. Allg. Chem.* **1994**, *620*, 1889–1897.

[3] K. Daub, G. Meyer, *Z. Anorg. Allg. Chem.* **2010**, *636*, 1716–1719.

[4] *X-RED32 1.26, X-SHAPE2 2.05, Crystal Optimisation for Numerical Absorption Correction*, Stoe & Cie. GmbH, Darmstadt, Germany, **2004**.

[5] G. M. Sheldrick, *SHELXS*, University of Göttingen, Germany, **1997**.

[6] G. M. Sheldrick, *SHELXL*, University of Göttingen, Germany, **1997**.

[7] G. Meyer, P. Ax, *Mater. Res. Bull.* **1982**, *17*, 1447–1455.

[8] M. D. Lyantaya, A. B. Goucharak, *Zh. Prikl. Khim.* **1971**, *44*, 1410–1412.

[9] R. Pöttgen, T. Gulden, A. Simon, *GIT Lab. J.* **1999**, *43*, 133–136.

[10] A. Simon, *J. Appl. Crystallogr.* **1970**, *3*, 11–18.

[11] P. Jeitschko, A. Simon, R. Ramlau, H. Mattausch, *Eur. Microscopy Microanal.* **1997**, *46*, 21.

[12] P. A. Stadelmann, *Ultramicroscopy* **1987**, *21*, 131–146.

Received: February 28, 2011